

PAPER • OPEN ACCESS

Patagonian toothfish-inspired aluminum coordination hydrogel sensors for real-time rainfall monitoring



To cite this article: Xiaoyu Guan *et al* 2025 *Int. J. Extrem. Manuf.* **7** 045502

View the [article online](#) for updates and enhancements.

You may also like

- [Potential of commercial microwave link network derived rainfall for river runoff simulations](#)
Gerhard Smiatek, Felix Keis, Christian Chwala et al.
- [Fabrication of bioactive conduits containing the fibroblast growth factor 1 and neural stem cells for peripheral nerve regeneration across a 15 mm critical gap](#)
Hsiao-Chiang Ni, Ting-Chen Tseng, Jeng-Rung Chen et al.
- [The Reliability of X-Band Multiparameter Radar Rainfall Estimates](#)
Q R Fajriani, R Jayadi, D Legono et al.

Patagonian toothfish-inspired aluminum coordination hydrogel sensors for real-time rainfall monitoring

Xiaoyu Guan^{1,3,*} , Yanxia Zhu¹, Jianxun Luo², Xuechuan Wang^{1,*}, Hao Gong¹, Mohammed A Abosheasha⁴, Bingyuan Zhang¹, Sai Zheng¹, Dongping Li¹, Qingxin Han^{1,*}, Motoki Ueda^{3,4} and Yoshihiro Ito^{3,4} 

¹ College of Bioresources Chemical and Materials Engineering, Institute of Biomass & Functional Materials, Shaanxi University of Science & Technology, Xi'an, Shaanxi 710021, People's Republic of China

² College of Materials and Textile Engineering, Jiaying University, Jiaying, Zhejiang 314001, People's Republic of China

³ Nano Medical Engineering Laboratory, RIKEN Cluster for Pioneering Research, 2-1 Hirosawa, Wako, 351-0198, Saitama, Japan

⁴ Emergent Bioengineering Materials Research Team, RIKEN Center for Emergent Matter Science (CEMS), 2-1 Hirosawa, Wako 351-0198, Saitama, Japan

E-mail: guanxiaoyu@sust.edu.cn, wangxc@sust.edu.cn and hanqingxin@sust.edu.cn

Received 21 October 2024, revised 23 November 2024

Accepted for publication 18 February 2025

Published 25 March 2025



Abstract

Compared with traditional rain gauges and weather radars, hydrogel flexible electronic sensor capable of responding directly to rainfall events with promptness and authenticity, shows great prospects in real-time rainfall monitoring. Aluminum coordination hydrogel (Al-HG), one of the most qualified sensors suitable for rainfall monitoring, however, is currently impeded from widespread application by its weak mechanical properties due to the low binding strength between Al^{3+} and functional ligands. Herein, inspired by the antifreeze proteins (AFPs) that protect those Patagonian toothfishes by strongly binding to ice crystals at freezing temperatures, a low temperature-induced strategy is introduced to promote more and stronger ligand carboxyls firm combination with Al^{3+} , thus forming a high-coordinated structure to deal with this challenge. Expectedly, the whole mechanical performance of the product $Al-HG_{F1/F2}$ obtained by the low temperature-induced strategy is improved. For example, the tensile fracture toughness and the maximum compressive stress of $Al-HG_{F1/F2}$ are $1.66 MJ \cdot m^{-3}$ and 12.01 MPa, approximately twice those of the sample $Al-HG_{F3/F0}$ obtained by traditional soaking method ($0.86 MJ \cdot m^{-3}$ and 7.38 MPa, respectively). Coupled with its good biocompatibility, ionic conductivity, and sensing ability, $Al-HG_{F1/F2}$ demonstrates promising application for real-time rainfall monitoring in discrepant rainfall intensities, different zones, and even under extreme environments. This work aims to offer a stride toward mechanically robust aluminum coordination hydrogel sensors for real-time rainfall monitoring as well as provide insights into flood prevention and disaster mitigation.

* Authors to whom any correspondence should be addressed.



Original content from this work may be used under the terms of the [Creative Commons Attribution 4.0 licence](https://creativecommons.org/licenses/by/4.0/). Any further distribution of this work must maintain attribution to the author(s) and the title of the work, journal citation and DOI.

Supplementary material for this article is available [online](#)

Keywords: aluminum coordination hydrogel, rainfall monitoring, mechanical performance, flexible electronic sensor, binding

1. Introduction

In the context of the growing frequency of dire weather events induced by global warming, real-time and accurate rainfall monitoring is essential for disaster prevention and mitigation, water resources management, and agricultural irrigation^[1–3]. Although the traditional rainfall monitoring methods, such as rain gauges and weather radars are effective, they might be limited in some applications by deployment cost, flexibility, or instantaneity. Therefore, it is particularly important to explore new and efficient rainfall monitoring technology.

In recent years, hydrogel materials that could transfer external stimulus into quantifiable electrical pulses have attracted extensive attention in the field of flexible electronic sensors, including wearable devices, virtual reality, and artificial intelligence^[4–6]. Interestingly, if the hydrogel bearing the sensing ability was used for rainfall monitoring, the impact of raindrops falling on the surface of the sensor can be converted into pressure changes inside the hydrogel, which can be further converted into measurable electrical signals, to achieve real-time monitoring of rainfall. The advantage of this method is that it can respond directly to the rainfall event itself, not just the humidity or moisture changes after the rainfall, demonstrating promptness and authenticity.

Among the conductive hydrogel sensors bearing conducting medium such as MXenes^[6], carbon black^[7], graphene oxide^[8], and metal salts^[9], metal coordination hydrogels, of which metal ions behave as conductive materials and polymer chains as flexible substrates, are conspicuous^[10,11]. Especially, aluminum coordination hydrogel (Al-HG) shows its unique application potential: (i) high charge density of aluminum ions enhancing the internal electric field of the hydrogel, thus speeding up ion conduction and charge transfer, thereby improving the sensitivity of the sensor; (ii) the abundance of aluminum offering a wide range of raw material sources and relatively low cost, conducive to its large-scale production and application; (iii) particularly, the good biocompatibility of aluminum ensuring its safety and sustainability of rainfall monitoring. However, one challenge still exists to impede the widespread application of Al-HG as an efficient sensor for rainfall monitoring.

According to the theory of coordination chemistry, for aluminum ions (Al^{3+}), the electron pairs of the functional ligands (exemplified by carboxyl) can only be put into the Al outer d orbitals with higher energy due to the nature of outer electron orbital structure of Al (sp^3d^2)^[12]. The binding force between the functional ligands and Al^{3+} is basically electrostatic attraction, i.e. ionic bonds or ion-dipole bonds are relatively dominant. Such a compound known as an outer-orbital complex is

inherently characterized by energy instability. Moreover, the water molecules would compete with functional ligands for Al^{3+} , generally leading to a uni-point fixation between Al^{3+} and target ligands. Such low binding strength was also proved by our previous work that was analyzed by first-principles calculations and molecular dynamics (MD) simulation: the direct contact distance between Al^{3+} and O (from carboxyl of PAA) was relatively long (approximate 5.4 Å) and the binding energy value was -1.69 eV^[12]. The weakest combination between Al^{3+} and functional ligands resulted in the weak mechanical performance of Al-HG comparison of Cr-HG, Zr-HG, or even Fe-HG. Therefore, to achieve high-performance rainfall monitoring Al-HG sensor that can be long-term stable operation in harsh environments, significant improvement of its mechanical properties is urgent. In our previous work^[13], inspired by the shutter closing and opening regulation mechanism, a method regulating the structure of hydrogel to facilitate Al^{3+} permeation for enhancing the mechanical performance of Al-HG was proposed. Nevertheless, the weak combination between Al^{3+} and functional ligands, dominantly impairing the mechanical property of Al-HG, never gets addressed.

As for modern scientific research, the bionics technique plays a vital role^[14–16]. Antarctic cod, also known as “Patagonian toothfish”, is the most cold-resistant fish in the world, able to survive and thrive in extremely low temperatures. Such tenacious vitality is largely due to special components in their blood, i.e. antifreeze proteins, which include antifreeze glycoprotein (AFGP) and four different types of antifreeze proteins (AFPs), weaving a protective net against extreme cold^[17–19]. For AFPs, each peptide chain has multiple sites that can bind specifically to ice crystals. When the ambient temperature drops below the freezing point, these sites are like magnets, attracting and firmly binding the surrounding ice crystal molecules, effectively preventing the disordered growth and expansion of ice crystals in the blood vessels and tissues of the fish body, thus maintaining the fluidity of the body fluid and the normal operation of physiological functions. The phenomenon that those sites of AFPs peptide chain are capable of strongly binding ice crystals upon temperature reaching the freezing point is magical. If the functional ligands in HG could be firm and multipoint combined with Al^{3+} under a low temperature, the success of solving the obstinate challenge of low binding strength thus weak mechanical performance of Al-HG would follow. Interestingly, such a hypothesis could be realized theoretically. According to Gibbs free energy theory, when the temperature decreases, the coordination binding appears to undergo a “strengthening” process, in which the loose coordination patterns become more stable, promoting the formation of high-coordinated structures^[20].

The antifreeze mechanism of Patagonian toothfish that the sites of its AFPs peptide chain could be able to strongly bind ice crystals upon temperature reaching the freezing point provides a new perspective on the synthesis of Al-HG with high coordination strength.

Herein, inspired by the Patagonian toothfish, an approving Al-HG_{F1/F2} with enhanced mechanical properties was fabricated by the low temperature induced strategy, which demonstrated promising application in real-time rainfall monitoring. Specifically, instead of the traditional method that ended the fabrication after soaking hydrogel (HG) in an Al³⁺ solution, this strategy continued to add a low-temperature treatment step. Compared with the product by the traditional method (Al-HG_{F3/F0}), the mechanical performances such as strength, toughness, puncture resistance, tear resistance, and other related properties of Al-HG_{F1/F2} were significantly promoted. The mechanism of low temperature promoting the formation of high-coordinated Al-HG_{F1/F2} was tried to decode by systematic technical characterization. After evaluation of sensing sensitivity/response/recovery time/stability, biocompatibility, and conductivity, the potential application of Al-HG_{F1/F2} in real-time rainfall monitoring was assessed. Therefore, the Patagonian toothfish-inspired low-temperature “strengthening” strategy provides a new perspective in hydrogel construction to narrow the gap between rainfall monitoring sensors and fragile Al-HG materials.

2. Experimental

2.1. Materials

Poly(vinyl alcohol) (PVA, purity >99%, $M_w \sim 750\ 000$), monomer acrylic acid (AA, purity >99%), monomer acrylamide (AM, purity >99%), ammonium persulfate (APS, purity $\geq 98\%$), *N, N'*-methylenebisacrylamide (MBAA, purity >99%), and aluminum chloride hexahydrate (AlCl₃·6H₂O, 99%) were purchased from Tianjin Kemiou Chemical Reagent Co., Ltd (China). The water used throughout the experiments was deionized water. All chemicals were used without further purification in this experiment.

2.2. Fabrication of aluminum coordination hydrogels (Al-HG_{F_x/F(3-x)})

The aluminum coordination hydrogel was synthesized by two methods. For the same step, a solution containing monomer AA (8 wt%), AM (8 wt%), PVA (10 wt%), initiator APS (0.25 wt%), and crosslinker MBAA (0.27 wt%) was prepared at 0 °C and then deoxygenated for 20 min using N₂. The solution was subsequently transferred into a mold for polymerization at 37.5 °C for 6 h, followed by freeze (−20 °C)-thawing (25 °C) for one cycle to obtain the pristine hydrogel (HG*, PVA/PAM-co-PAA). Herein, PAM-co-PAA served as the soft phase and PVA as the hard phase, endowing the hydrogel with a simple preparation process as well as good overall performance. Specifically, the PAA component offered the mainly functional ligands (−COOH) to capture

Al³⁺. For traditional aluminum coordination hydrogel, HG* continually underwent two more freeze-thaw cycles, obtaining HG, and then HG was immersed in an Al³⁺ solution with a concentration of 0.06 mol·L^{−1} at 25 °C for 12 h, forming Al-HG_{F3/F0}. For the low temperature induced aluminum coordination hydrogel, two strategies were used: (i) HG* continually undergoing one cycle of freeze-thaw, then soaking in the Al³⁺ aqueous solution, and finally undergoing one more cycle of freeze-thaw, forming Al-HG_{F2/F1}; (ii) HG* soaking in the Al³⁺ aqueous solution first, and then undergoing two cycles of freeze-thaw, forming Al-HG_{F1/F2}. Overall, the aluminum coordination hydrogel could be named Al-HG_{F_x/F(3-x)}. Herein, *x* indicated the number of freeze-thaw cycles performed before Al³⁺ soaking, while 3-*x* was the number of freeze-thaw cycles carried out after Al³⁺ soaking. For all samples, the total number of freeze-thaw cycles was controlled at 3. During the fabrication process of Al-HG_{F2/F1} and Al-HG_{F1/F2}, freeze-thaw treatment was applied in two stages, including before and after Al³⁺ soaking. Before Al³⁺ soaking was the aim of forming the pristine hydrogel by generating PVA crystalline domains and hydrogen bonds among the functional groups of −NH₂, −COOH, and −OH. After Al³⁺ soaking was in order to strengthen the aluminum coordination hydrogel by forming high-coordinated structure. The fabrication process of Al-HG_{F_x/F(3-x)} was further illustrated in Figure S1.

2.3. Mechanical property testing

The mechanical performance of the hydrogels was tested using a machine (CMT6503, MTS, USA) at 25 °C. For the tensile experiment, the hydrogel was made into dumbbell-type (21 mm × 2 mm × 2 mm) according to the national standard dumbbell cutting dimensions, which was conducted at 100 mm·min^{−1} tensile speed with a 100 N load. The toughness of hydrogel was determined by calculating the area under the tensile stress-strain curve, and Young's modulus was obtained from the slope of the initial linear portion of the stress-strain curve. For the notched tearing tensile experiment, the sample was initially cut into rectangular shapes with dimensions of 30 mm in length, 10 mm in width, and 2 mm in thickness. Meanwhile, a 2 mm pre-notch was introduced at the edge.

For compression tests, the samples were prepared to be cylindrical ($d = 20\ \text{mm}$, $h = 10\ \text{mm}$), and performed at a speed of 5 mm·min^{−1} with a load of 500 N. For puncture tests, hydrogels were made into 10 mm diameter, 2 mm thick columns, and were punctured by using a needle with a 1 mm radius. All the tests were performed five times, and the average with standard deviations was recorded.

The rheological measurements were performed on a TA DHR-1 rheometer (USA) using a 20 mm parallel plate. Frequency sweeps of the samples were performed at a constant strain of 1% at 25 °C, with frequencies from 0.1 to 100 rad·s^{−1}.

The mass of the hydrogel drying in an oven at 40 °C to a constant weight was recorded as W_d , and the mass of the swollen hydrogel was measured as W_s after removing excess surface water with filter paper. The swelling ratio (SR) was

determined using the formula:

$$SR = \frac{W_s - W_d}{W_d} \times 100\% \quad (1)$$

The mass of hydrogel before drying was recorded as W_0 , and its mass after drying in an oven at 40 °C to a constant weight was determined as W_d . The water content (WC) of the hydrogel can be calculated using the equation:

$$WC = \frac{W_0 - W_d}{W_d} \times 100\% \quad (2)$$

2.4. Structural characterization

The morphology of the hydrogel samples after freeze-drying was obtained using ZEISS Gemini 360 Field-Emission Scanning Electron Microscopy (SEM, Germany). The elemental distribution in the composite hydrogels was observed with Oxford instruments Energy-Dispersive Spectroscopy (EDS, UK). X-ray photoelectron spectroscopy (XPS) was obtained by an AXIS SUPRA apparatus (United Kingdom) at the step size of 1.00 eV in the range of 0 – 1 100 eV. Fourier transforms infrared (FTIR) was carried out using a Thermo Scientific Nicolet 5700 FTIR spectrometer (USA), providing spectra over a range from 400 to 4 000 cm^{-1} . X-ray diffraction (XRD) patterns were obtained using a Philips X'Pert pro-MPD diffractometer, by Cu-K α radiation ($\lambda = 1.5406 \text{ \AA}$) over a range from 5° to 60°. The SAXS (Small Angle x-ray Scattering) was done by the Anton Paar SAXSpoint 2.0 (Austria).

2.5. Application of Al-HG_{F1/F2} in real-time rainfall monitoring

Before application, the biocompatibility (using NIH-3T3 cells, Procedure S1 and S2) and the ionic conductivity (Procedure S3) were assessed. The flexible electronic sensing performance of Al-HG_{F1/F2} under different strains and pressures was evaluated by the relative resistance changes, which were measured using a tensile machine (CMT6503, MTS, USA) combined with the Keithley2450 digital source meter (USA). For strain-responsive sensors, the two metal wires as electrodes were connected on both sides of the samples (20 mm × 5 mm × 2 mm) to fabricate the assembly as ionic conductors. For pressure-responsive sensors, the size of cylindrical gel sensors as ionic conductors was $d = 20 \text{ mm}$ and $h = 2 \text{ mm}$. Relative resistance change (l) was determined by the formula:

$$l = \frac{(R - R_0)}{R_0} \times 100\% \quad (3)$$

in which R_0 and R were the initial and tested resistance of the hydrogel, respectively.

The Gauge Factor (GF) was employed to evaluate the sensitivity during the process of stretching hydrogels, calculated by the formula:

$$GF = \frac{l}{\varepsilon} \quad (4)$$

where ε is the applied strain.

The sensitivity (S) was employed to assess the sensitivity of hydrogels during the compressive process, obtained by the formula:

$$S = \frac{l}{\sigma} \quad (5)$$

where σ denoted the applied stress.

For application in rainfall monitoring, the Al-HG_{F1/F2} sample was mounted as the sensing elements on a roof model, with copper wires secured to both ends by insulating tape, and these wires were connected to a Keithley 2450 digital source meter. The rainwater solution was first simulated according to the common rainwater components, containing SO_4^{2-} ($1.21 \times 10^{-4} \text{ mol}\cdot\text{L}^{-1}$), NO_3^- ($1.32 \times 10^{-5} \text{ mol}\cdot\text{L}^{-1}$), NH_4^+ ($1.79 \times 10^{-5} \text{ mol}\cdot\text{L}^{-1}$), and Ca^{2+} ($3.50 \times 10^{-5} \text{ mol}\cdot\text{L}^{-1}$). Also, the different areas of rainwater in China including Xi'an, Heilongjiang, Beijing, Zhejiang, and Hubei were collected. The simulated rainfall was conducted by using a custom-made dripping system, and different rainfall intensities including light, moderate, heavy, and torrential rain, were represented by varying the height and droplet size. The real-time rainfall monitoring by Al-HG_{F1/F2} was carried out on the campus of Shaanxi University of Science and Technology, Xi'an, China, by evaluating the relative resistance changes.

3. Results and discussion

3.1. Fabrication of Al-HG_{F1/F2} inspired by Patagonian toothfish

Patagonian toothfish, the hardest fish in the world, is one of the most iconic creatures in the Antarctic Ocean. As demonstrated in Figure 1(a), Patagonian toothfish could live hundreds of meters below the ice in ocean depths, not only not being frozen, but also surviving and thriving normally. In addition to the morphological characteristics of Patagonian toothfish adapted to the cold environment, it also has remarkable freezing resistance due to the antifreeze proteins (AFPs) existing in its blood. The AFPs molecules have multiple sites where they can bind to ice crystals (Figure 1(b)). These sites are usually located on specific domains that are rich in hydrogen bond donors and receptors. When the temperature drops below the freezing point, AFPs could strongly interact with the surface of ice crystals, thus preventing the freezing of body fluids. As a result, even when the water temperature is several degrees below zero or lower, the body fluids of Patagonian toothfish do not freeze, ensuring the normal functioning of its physiological functions. Inspired by the anti-freezing mechanism of Patagonian toothfishes that their sites of AFPs peptide chain are capable of strongly and multipoint binding ice crystals upon temperature reaching the freezing point, herein, a low temperature-induced aluminum coordination hydrogel (Al-HG_{F1/F2}) was fabricated. In detail (Figure 1(c)), AM/AA were as reaction monomers and APS as initiator, which were gelled by polymerization based on hydrogen bonding as well as MBAA crosslink bonding. PVA, as another network, enhanced the gel system by freezing/thawing operation endowing with abundant hydrogen

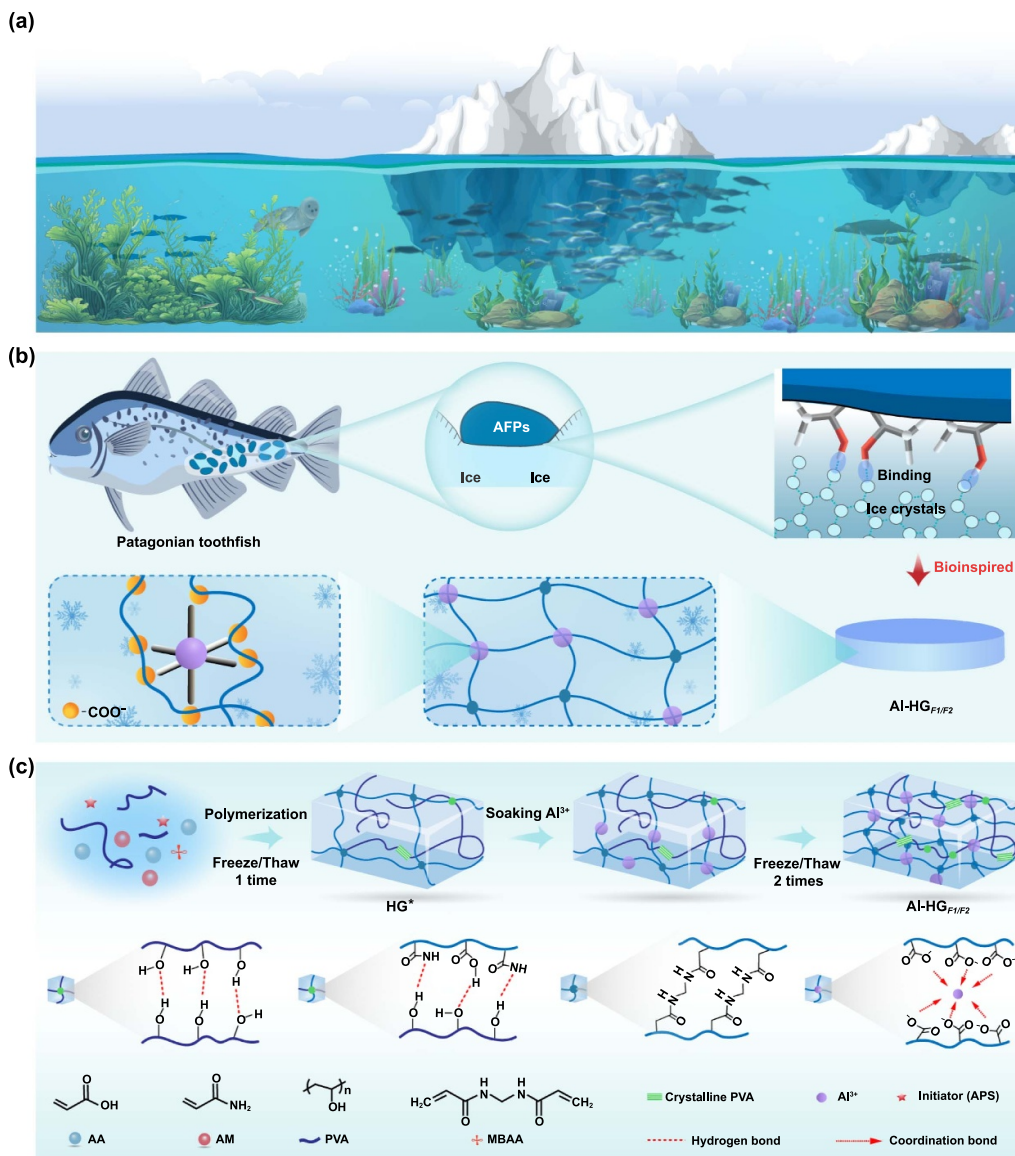


Figure 1. The fabrication of the present hydrogels inspired by Patagonian toothfish: (a) the scheme of fishes living in the Antarctic Ocean, (b) the fabrication of the specific aluminum coordination hydrogel (Al-HG_{F1/F2}) inspired by the function of the antifreeze proteins (AFPs) existing in the Patagonian toothfish, (c) the scheme of the fabrication and gelation mechanism of Al-HG_{F1/F2}.

bonds among $-OH$, $-COOH$, and $-NH_2$. Specifically, instead of the traditional method that ended the fabrication after soaking hydrogel in an Al^{3+} solution, the present strategy continued to add a low-temperature treatment step, i.e. freezing/thawing operation repeated 2 times. Inspired by the anti-freeze mechanism of Patagonian toothfish and combined with Gibbs free energy theory, the assumption of low temperature-induced strategy could intensify the coordination between Al^{3+} and the functional $-COO^-$, promoting the formation of high-coordinated structures. For example, the strong ligands $-COO^-$ could supersede more water molecule weak ligands, manifesting as high-coordinated structures formation (such as six-coordinated), not the commonly single point coordination.

3.2. Comparison of mechanical properties of Al-HG_{Fx/F(3-x)}

To prove that the low temperature induced strategy is effective, in this part, the mechanical properties of four samples, hydrogel before Al soaking (HG), Al-HG prepared by the traditional method (Al-HG_{F3/F0}), and Al-HG obtained by the low temperature induced strategy (Al-HG_{F1/F2}, Al-HG_{F2/F1}) were systematically compared, which included tensile, compression, swelling behaviors, and so on. First, the samples were stretched to fracture to evaluate their tensile properties (Figure 2(a)). The curves of stress-strain (Figures 2(a-i)) demonstrated that the tensile mechanical property of all Al-HG samples was superior to that of the HG. That's why numerous studies introduced metal ions such as Al^{3+} , Fe^{3+} ,

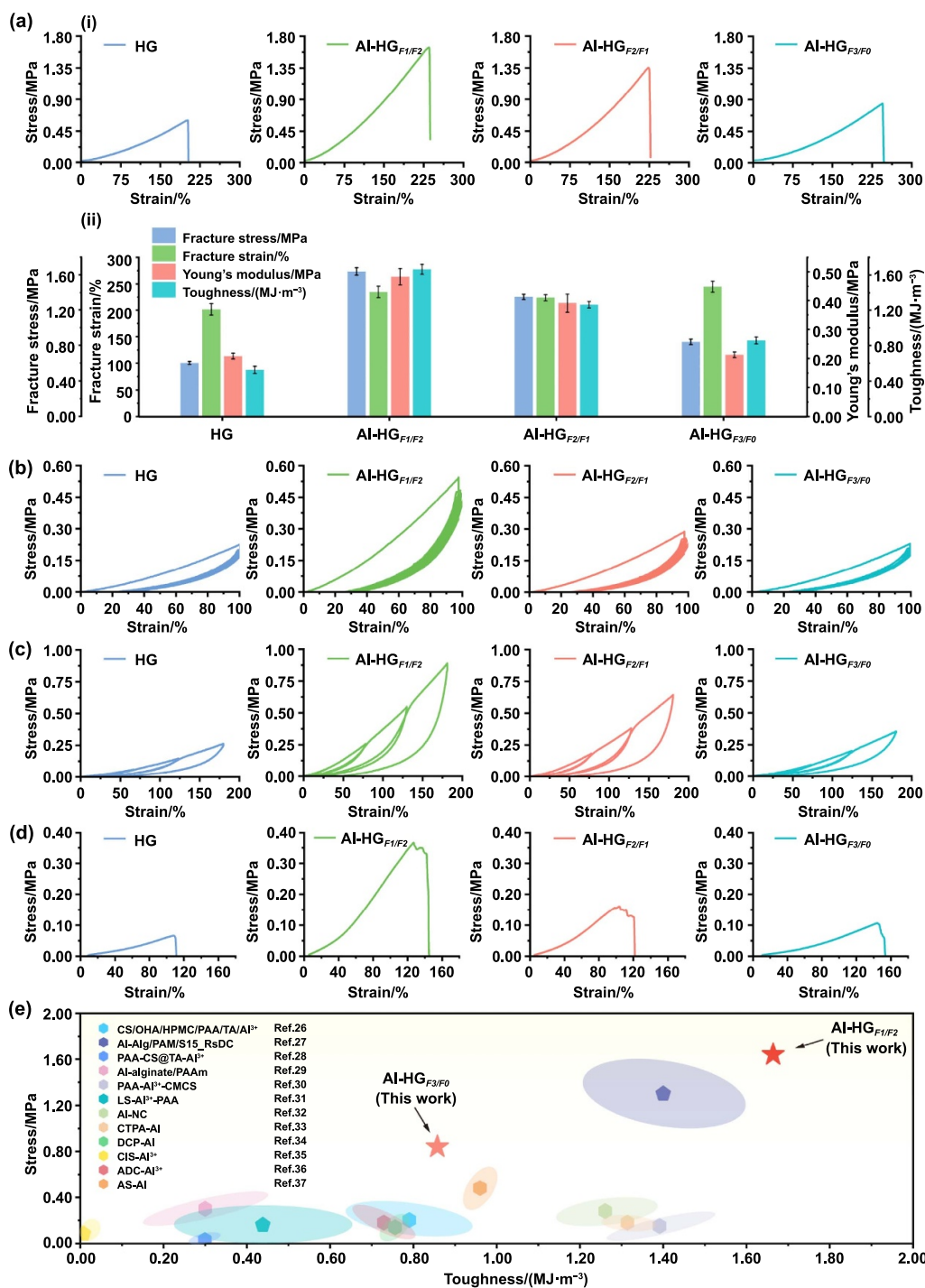


Figure 2. Tensile property of samples: (a) single tensile performance (i) stress-strain curves and (ii) their detailed mechanical property values, (b) twenty loading-unloading curves at 100% strain, (c) cyclic loading-unloading curves with gradually increasing strain, (d) tearing curves, (e) the comparison of the stress and toughness with those of previously reported aluminum coordination hydrogels.

Zr⁴⁺, Ln³⁺, etc. into the hydrogel to enhance the mechanical property based on the mechanism of energy dissipation^[21–25]. Moreover, for Al-HG samples, it could be found that the tensile property of the Al-HG_{F1/F2} was the best and Al-HG_{F3/F0} was the weakest, indicating the effectiveness of the low temperature-induced strategy. For further quantitative comparison, the values of tensile fracture strain (%), fracture stress (MPa), Young's modulus (MPa), and toughness

(MJ·m⁻³), derived from the corresponding tensile curves, were illustrated in Figure 2(a-ii) and summarized in Table S1. It showed that the whole tensile mechanical property of Al-HG_{F1/F2} was the best. Taking the aggregative indicator, toughness, as an example, it was 1.66 MJ·m⁻³ for Al-HG_{F1/F2}: approximately twice that of the Al-HG_{F3/F0} (0.86 MJ·m⁻³) and also significantly higher than that of the Al-HG_{F2/F1} (1.26 MJ·m⁻³). Both Al-HG_{F1/F2} and Al-HG_{F2/F1}

were obtained by low temperature induced strategy, and the difference between them was two cycles of freeze-thaw after Al^{3+} soaking of $\text{Al-HG}_{F1/F2}$ sample, while one cycle of freeze-thaw for $\text{Al-HG}_{F2/F1}$. The better mechanical properties of $\text{Al-HG}_{F1/F2}$ than that of $\text{Al-HG}_{F2/F1}$ indicated that only one cycle of freeze-thaw was not enough to intensify the coordination bonds between Al^{3+} and functional ligands. It was worth noting that for $\text{Al-HG}_{F3/F0}$ and HG samples, the fracture strains were prominent compared with their other mechanical properties such as Young's modulus, fracture stress, and toughness. The fracture strain of $\text{Al-HG}_{F3/F0}$ (244.80%) was even superior to that of $\text{Al-HG}_{F1/F2}$ (234.61%). This phenomenon was attributed to more low-strength coordination bonds (also called ionic bonds or ion-dipole bonds) and hydrogen bonds existence in $\text{Al-HG}_{F3/F0}$ and HG samples.

Subsequently, the fatigue durability was evaluated by twenty cycles of loading-unloading tensile tests at 100% strain (Figure 2(b)). As for the first loading-unloading curve, all the samples exhibited significant hysteresis. The hysteresis phenomenon was attributed to energy dissipation caused by the breaking of hydrogen or coordination bonds during deformation. It was known that the area covered by the first loading-unloading curve was denoted the dissipated energy. Therefore, the sample of $\text{Al-HG}_{F1/F2}$ showed the most obvious energy dissipation, manifesting as the largest covered area of its first loading-unloading curve. This result proved that the low-temperature induced method could improve energy dissipation, thus enhancing its toughness. As the number of cycles increased, the curves were almost completely overlapped, demonstrating that the samples had good structural recovery and fatigue resistance. Additionally, the cyclic loading-unloading curves at different strains (Figure 2(c)) showed that the dissipated energy was positively correlated with its tensile strain, especially for the $\text{Al-HG}_{F1/F2}$ sample, indicating that the multiple physical or chemical interactions within the hydrogel network could effectively dissipate energy. This confirmed the mechanical stability and durability of the hydrogels under long-term repetitive stress. To evaluate the application value of samples with minor ruptures for rainfall monitoring, these samples were subjected to tear tensile tests with identical notches to obtain their stress-strain curves (Figure 2(d)). The results showed that, despite the overall performance of the notched hydrogel was lower than that of the intact one (Figure 2(a)), the $\text{Al-HG}_{F1/F2}$ sample still demonstrated superior performance compared to the HG, $\text{Al-HG}_{F2/F1}$, and $\text{Al-HG}_{F3/F0}$ samples. Furthermore, as shown in Figure 2(e), the tensile properties (e.g. stress and toughness) of $\text{Al-HG}_{F3/F0}$, prepared using the traditional soaking method, were comparable to those of most reported Al-HG ^[26–37]. Expectedly, both the stress and toughness of the $\text{Al-HG}_{F1/F2}$ sample were significantly superior to them. This remarkable result indicated that the low temperature-induced strategy held promise for significantly enhancing the mechanical properties of Al-HG . Moreover, to evaluate the general applicability of this method, Zr^{4+} and Fe^{3+} were employed as alternative objects. Their tensile curves (Figure S2) showed that the

low temperature-induced $\text{Fe-HG}_{F1/F2}$ and $\text{Zr-HG}_{F1/F2}$ exhibited higher strength compared to the $\text{Fe-HG}_{F3/F0}$ and $\text{Zr-HG}_{F3/F0}$ samples prepared by the traditional soaking method. However, this increase in the strength of Zr-HG and Fe-HG samples came at the expense of some strain. But the aggregative indicator, the toughness of $\text{MI-HG}_{F1/F2}$ was slightly better than that of $\text{MI-HG}_{F3/F0}$, indicating that the low temperature-induced strategy had a certain level of general applicability. It is worth noting that, nonetheless, the low temperature-induced method was the most suitable for fabricating Al-HG , which was proved by the calculation of the enhancement ratio of the mechanical properties of Fe, Zr, and Al -coordination hydrogels prepared by the low temperature-induced strategy compared with the traditional soaking method (Figure S3). For example, the toughness enhancement ratio (%) of Fe-HG , Zr-HG , and Al-HG was 11.3%, 11.4%, and 94.1%, respectively. Such phenomenon that low temperature could significantly strengthen the coordination strength between Al and functional ligands was as expected due to the nature of the outer electron orbital structure of Al (i.e. in its initial state, more water molecules rather than functional ligands coordination with Al^{3+}).

In this section, their compressive property, rheological property, and swelling ratio were further compared. According to the compressive stress-strain curves (Figure 3(a)), it could be found that, similar to the tensile property, the $\text{Al-HG}_{F1/F2}$ sample also achieved a significantly improved compressive property. The maximum compressive strength value (at 90% strain), reflecting the hydrogel's load-bearing capacity under high compressive deformation, an important parameter for evaluating its compressive property, was summarized in Table S2. The maximum compressive stress of $\text{Al-HG}_{F1/F2}$ was 12.01 MPa, approximately two times of that $\text{Al-HG}_{F3/F0}$ sample (7.38 MPa), about six times of that HG (2.17 MPa), indicating the effectiveness of low temperature-induced strategy increased the compressive property. To evaluate the compressive stability and durability, the samples were subject to twenty cycles of loading-unloading at 60% strain (Figure 3(b)), and the maximum compressive stress according to their stress-strain curves was illustrated in Figure 3(c). It could be found that, in addition to having maximum compressive strength at 60% strain (about 0.8 MPa), the repeated stresses of the $\text{Al-HG}_{F1/F2}$ sample remained stable (Figure 3(c)), indicating a good fatigue resistance, which was crucial for the application of hydrogels in real-time rainfall monitoring, especially when exposed to rainwater environments over long periods. In addition, the small area of the hysteresis loop (Figure 3(b)) indicated that the hydrogel dissipated little energy during the cyclic loading-unloading process at 60% strain, demonstrating high energy dissipation capacity. Subsequently, the puncture test was used to further evaluate the hydrogel's puncture resistance, particularly under localized concentrated stress. According to the puncture force-displacement curves (Figure 3(d)), as expected, the $\text{Al-HG}_{F1/F2}$ sample showed the best puncture resistance, with puncture force (11.07 N) approximately twice that of the $\text{Al-HG}_{F3/F0}$ sample (5.79 N) and four times that of the HG sample

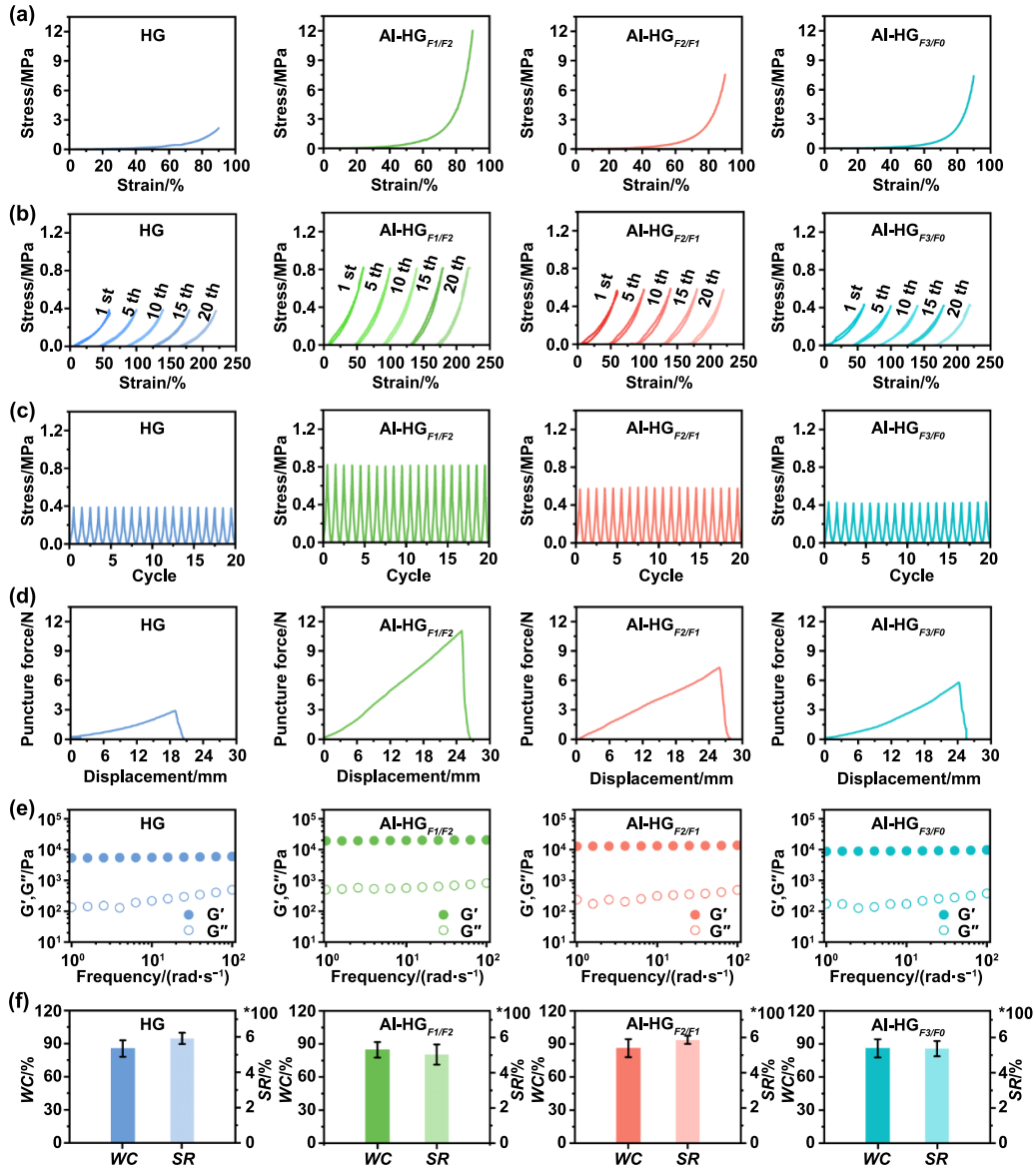


Figure 3. Compressive and other properties of samples: (a) stress-strain curves at 90% strain, (b) twenty cycles of loading-unloading stress-strain curves at 60% strain, (c) the stress values of the twenty cycles of loading-unloading at 60% strain, (d) puncture force-displacement curves, (e) rheological property determined by storage modulus (G') and loss modulus (G''), (f) the water content (WC) and the swelling ratio (SR) of samples.

(2.88 N). This indicated that the Al-HG_{F1/F2} had higher surface strength and excellent structural stability, providing stronger impact resistance in practical real-time rainfall monitoring applications.

Moreover, the viscoelastic property, indirectly indicating its mechanical performance, was evaluated through rheological testing by analyzing the storage modulus (G') and loss modulus (G''). G' represents the energy stored during elastic deformation, reflecting the elastic behavior of the material, while G'' indicates the energy dissipated during flow, representing its viscous behavior^[38–41]. When $G' > G''$, it indicates an elastic characteristic of the material, behaving similarly to a solid. As shown in Figure 3(e), across the entire frequency range, the G' values of all four samples were higher than their G'' values, confirming their elastomers. Additionally,

the low-frequency dependence of G' indicated that the structure of the samples remained stable, with minimal relaxation. Significantly, the whole frequencies G' values of the Al-HG_{F1/F2} obtained by low temperature induced strategy were higher than those of the HG, Al-HG_{F2/F1}, and Al-HG_{F3/F0} samples. In general, a higher G' value suggests that the material has superior elasticity, greater rigidity, stronger structural stability, and better recovery capability under mechanical loads, further indicating the good mechanical performance of Al-HG_{F1/F2}. Finally, the water content (WC) and swelling ratio (SR) that are closely related to the mechanical properties were discussed (Figure 3(f)). As a whole, the values of their WC were almost the same, approximately 85%, while the SR value of Al-HG_{F1/F2} was the lowest, which might be due to the stronger coordination between Al³⁺ and carboxyl

groups, thus leading to a more compact and ordered internal structure, making it more difficult for water molecules to penetrate, thereby effectively suppressing swelling. Moreover, as more carboxyl groups were coordinated by Al^{3+} , the electrostatic repulsion between the polymer chains of the hydrogel decreased^[13], which was another reason for the reduced swelling ratio of $\text{Al-HG}_{F1/F2}$. All the above results validated the effectiveness of the low temperature-induced strategy, obtaining the $\text{Al-HG}_{F1/F2}$ with good stability under multiple mechanical loads and in aqueous environments.

3.3. Analysis of the mechanism for the promoted mechanical property by low temperature-induced strategy

The above results proved that the $\text{Al-HG}_{F1/F2}$ sample, fabricated via low-temperature induction, exhibited the best tensile, compressive, puncture resistance, and anti-swelling properties, demonstrating excellent overall mechanical performance. Herein, the mechanism for the promoted mechanical property by low temperature induced strategy was tried to confirm by system characterization from macro to micro scales. First of all, the macroscopic appearance of the four samples could be observed by their digital photographs. As could be seen in Figure 4(a), the sample of HG showed high transparency, which was ascribed to the refractive index of present hydrophilic polymers ($\sim 1.40\text{--}1.60$) close to that of water (1.33)^[42,43]. In contrast, the transparency of $\text{Al-HG}_{F3/F0}$, after Al^{3+} introduction, was slightly reduced. Significantly, by the low temperature induced strategy, the product, especially the $\text{Al-HG}_{F1/F2}$ sample, exhibited the lowest transparency. Such a phenomenon might be attributed to more ligands of bound water in $\text{Al-HG}_{F1/F2}$ hydrogel being superseded by the functional ligands of carboxyl groups. On the other hand, the volume of the $\text{Al-HG}_{F1/F2}$ was the smallest, the result of which was consistent with that of its swelling ratio (Figure 3(f)). Subsequently, their microstructures were distinguished by SEM technology. As shown in Figure 4(b), the HG sample displayed a complex surface morphology with dense regions and irregular pore distributions, while the $\text{Al-HG}_{F3/F0}$ exhibited a rougher surface and smoother pore structure primarily due to the coordination bonding between Al^{3+} and carboxyl groups, thus reducing the polymer chain space and decreasing the pore size. Notably, the $\text{Al-HG}_{F1/F2}$ sample showed a highly ordered fibrous micropore structure, which was attributed to the low temperature inducted strategy, promoting the formation of more and concordant high-coordinated structures, thus exhibited the smallest macroscopic volume (Figure 4(a)) and the highest strength and toughness (Figure 2(a)). Additionally, the high porosity of the fibrous structure increased light scattering, which was another reason for the lowest transparency of $\text{Al-HG}_{F1/F2}$ (Figure 4(a)). In comparison, the $\text{Al-HG}_{F2/F1}$ sample had more uniform pores, a denser overall network structure, and provided a certain degree of mechanical support, with its mechanical properties falling between those of $\text{Al-HG}_{F1/F2}$ and $\text{Al-HG}_{F3/F0}$, but slightly inferior to $\text{Al-HG}_{F1/F2}$.

The crystalline structure was further analyzed by x-ray diffraction (XRD) patterns (Figure 4(c)). The sharp peak at 20° was ascribed to the (200) and (101) planes of PVA, while

the peak at 41° was associated with the amorphous diffraction of PAM or diffraction reflection of PVA^[44]. Significantly, the peak at 20° of Al-HG was decreased compared with that of HG, indicating that the formation of coordination bonds decreased the crystallinity of PVA. Moreover, for $\text{Al-HG}_{F1/F2}$, $\text{Al-HG}_{F2/F1}$, and $\text{Al-HG}_{F3/F0}$, the peaks at $2\theta = 20^\circ$ of $\text{Al-HG}_{F1/F2}/\text{Al-HG}_{F2/F1}$ were slightly weaker than that of $\text{Al-HG}_{F3/F0}$, which might be due to the formation of high-coordinated structures, thus further leading to a decrease of PVA crystallinity, providing new evidence for the enhancement of mechanical performance by the low temperature-induced strategy. The above result regarding the crystallinity could be further corroborated by differential scanning calorimetry (DSC) data (Figure S4) that the crystallinity of HG, $\text{Al-HG}_{F1/F2}$, $\text{Al-HG}_{F2/F1}$, and $\text{Al-HG}_{F3/F0}$ was calculated to be 0.70%, 0.60%, 0.63%, and 0.66%, respectively^[45,46].

The chemical structure of them was determined by FTIR. As shown in Figure 4(d), the peaks at 2 920/2 848, 1 706, 1 647, and 979 cm^{-1} corresponded to C–H/N–H stretching vibrations, C=O stretching vibrations of carboxyl groups in PAA, N–H bending vibrations in MBAA or PAM, and C–O stretching vibrations in PVA, respectively^[13,47–49]. In comparison with the HG sample, the characteristic peaks at 2 920/2 848 and 1 647 cm^{-1} of the $\text{Al-HG}_{F1/F2}$, $\text{Al-HG}_{F2/F1}$, and $\text{Al-HG}_{F3/F0}$ were more distinct, which might be due to the formation of coordination bonds altering and enhancing the N–H bending vibration frequency.

Based on the above results, the structural model for them was proposed. As illustrated in Figure 4(e), the structure of HG was primarily stabilized by hydrogen bonds among –COOH, –NH₂, and –OH along the polymer chains. After soaking, the Al^{3+} ions were bonded by ligands (including –COO[–], H₂O, and Cl[–]) through coordination bonds. However, due to the nature of the outer electron orbital structure of Al, generally, only one electron pair of the functional carboxyls could be put into the Al outer *d* orbitals by the traditional soaking method, manifesting as a uni-point fixation between Al^{3+} and –COO[–] of $\text{Al-HG}_{F3/F0}$ sample (the other orbitals of Al were occupied by weak ligands such as H₂O and Cl[–]). By the low-temperature treatment, the strong ligand carboxyls would compete with weak ligands to capture the orbitals of Al, forming double- or even three-point fixation between Al^{3+} and –COO[–], exemplified by the $\text{Al-HG}_{F2/F1}$ sample. When enhanced low-temperature operation, the functional –COO[–] from the same or adjacent chains could forcibly occupy all the orbitals of Al, manifesting as the high-coordinated structure formation (such as six-coordinated) of the $\text{Al-HG}_{F1/F2}$ sample. Such a phenomenon was like those sites of AFPs peptide chain of Patagonian toothfish capable of strongly binding ice crystals upon temperature reaching the freezing point, i.e. the ligands –COO[–] function as the AFPs sites, while Al complexes as the ice crystals. On account of the more and stronger ligand carboxyls firmly binding Al^{3+} after the low-temperature treatment, the obstinate challenge of the low binding strength of traditional Al-HG was successfully solved, thus significantly improving its mechanical performance.

The above results indicated that the $\text{Al-HG}_{F1/F2}$ sample bearing with ordered fibrous micropore and high-coordinated

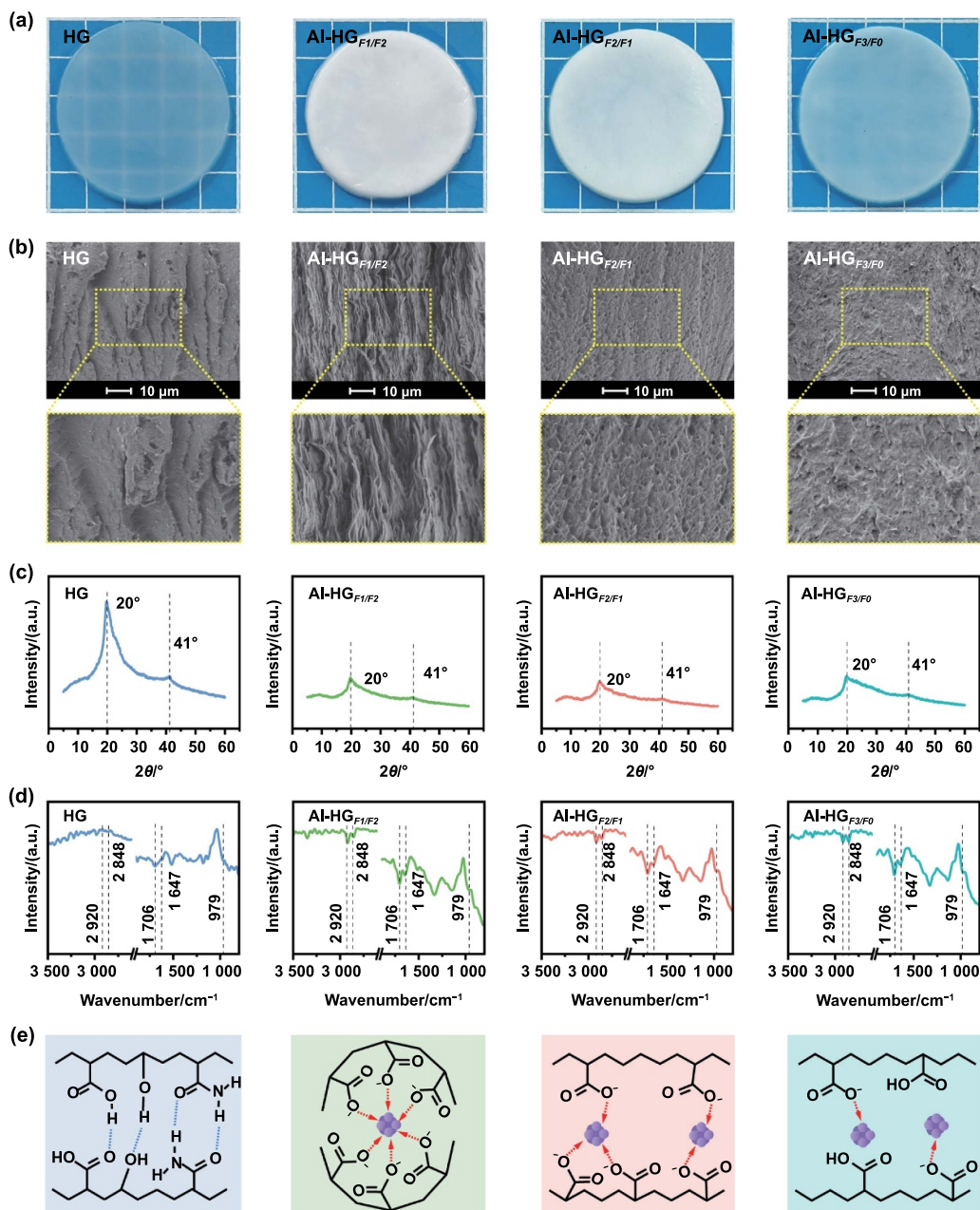


Figure 4. The microstructure and macroscopic of samples: (a) the digital pictures, (b) SEM images, (c) XRD patterns, (d) FTIR spectra, and (e) the major structure of HG and Al-HG_{F₁/F₂} (x including 1, 2, and 3, the coordination by the weak ligands such as H₂O and Cl⁻ was omitted).

structures exhibited improved and excellent mechanical properties. In this section, the elemental distribution, surface chemical states, and nanoscale structural features of Al-HG_{F₁/F₂} were characterized to further decipher the enhanced mechanical property of low temperature-induced strategy. First of all, the Al-HG_{F₁/F₂} mainly included four elements of C, O, Al, and N, with respective weight contents (wt%) of 65.3%, 27.4%, 5.0%, and 2.3% (figure 5(b)). The high C content was attributed to the carbon skeleton of the PVA, PAA, and PAM polymer chains. Although the N element could come from both PAM and MBAA, its content was lower than that of Al, indicating that a low temperature-induced strategy could facilitate Al being captured to form more coordination bonds. In the

EDS line scanning (Figure 5(d)), the concentrations of these elements showed minimal variation along the scanning line, with no significant transition regions. The uniform distribution of these elements was further proved by the EDS map scanning of these four elements (Figure 5(e)) and total elements (Figure 5(c)). In particular, the well-proportioned distribution of Al element, thus being stressed uniformly was another reason for Al-HG_{F₁/F₂} bearing a good mechanical performance. Subsequently, the surface chemical states of these elements in the Al-HG_{F₁/F₂} sample were analyzed by XPS (Figure 5(f)). The C 1s spectrum consisted of three peaks corresponding to C=O (287.4 eV), C-O (285.4 eV), and C-C/C-H (284.0 eV), with the main C-C/C-H peak arising from the

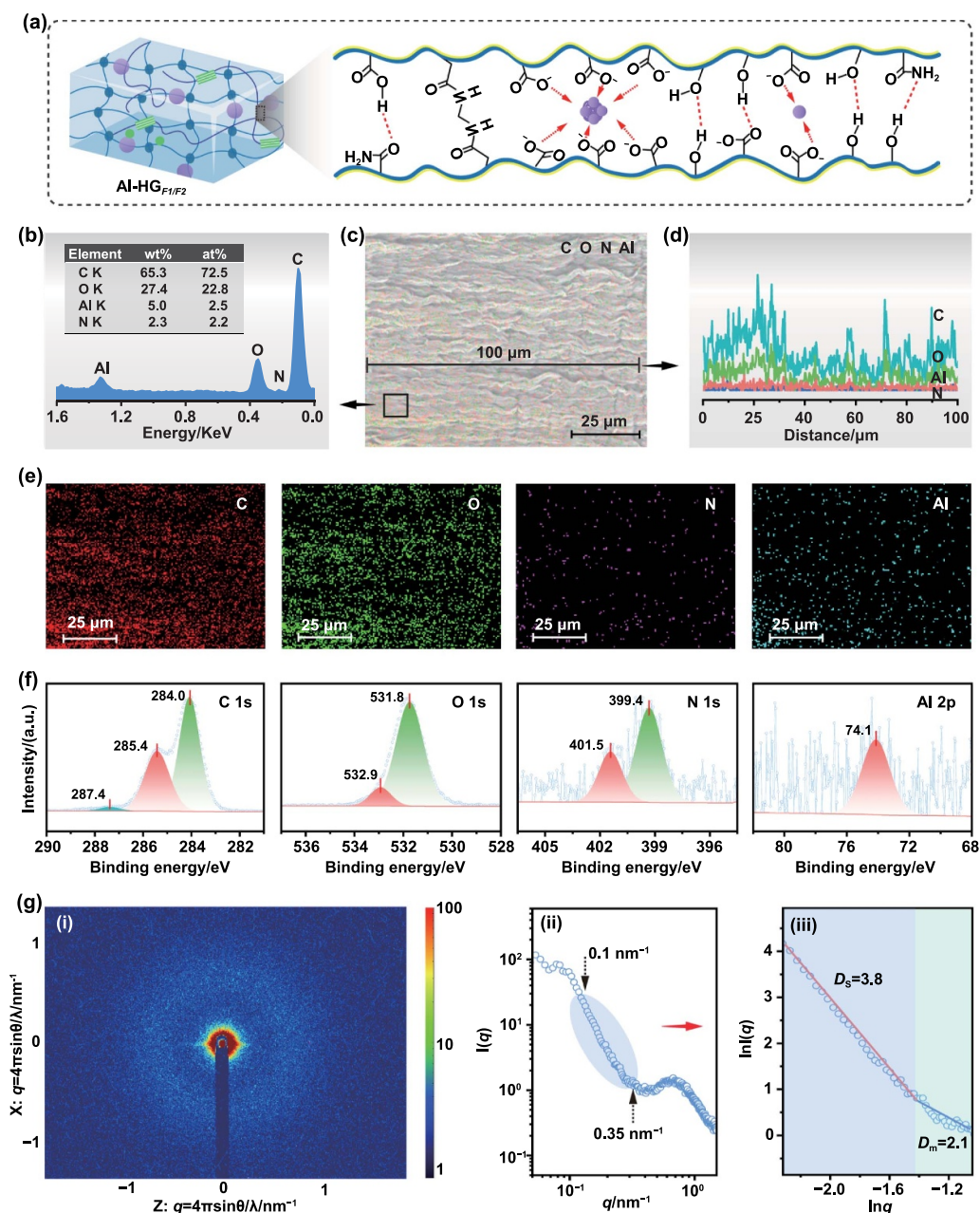


Figure 5. The chemical structure and elemental distribution of the Al-HG_{F1/F2} sample: (a) the chemical structure, (b) the EDS spectrum and content of the element, (c) EDS map scanning for all elements, (d) EDS line scanning of the four elements, (e) EDS map scanning of the four elements, (f) XPS high-resolution spectra of N 1s, C 1s, O 1s, and Al 2p, (g) SAXS results, (i) 2D SAXS pattern and (ii) the 1D profile plot of SAXS and (iii) corresponding fractal dimension.

polymer backbone. The O 1s spectrum exhibited two binding energy peaks, C=O (532.9 eV) and C–O–H (531.8 eV). The N 1s spectrum showed two peaks at 401.5 eV (associated with the amide group) and 399.4 eV (related to the amino group). The Al 2p spectrum peaked at 74.1 eV, indicating that Al formed stable coordination bonds with oxygen-containing groups (Al–O), consistent with its role as the coordination center. The above results revealed the internal chemical structure of the hydrogel (Figure 5(a)), which included multiple cross-linking networks twining by covalent bonds, hydrogen bonds, and Al coordination bonds, thus conferring superior mechanical properties to the Al-HG_{F1/F2}. Finally,

the nanostructural features of the Al-HG_{F1/F2} sample were explored by using SAXS technology (Figure 5(g)). The clear isotropic circular feature was observed in the 2D SAXS patterns (Figures 5(g–i)), indicating a highly isotropic structure at the microscopic scale^[50,51]. Based on the pattern, a 1D SAXS profile (Figure 5(g–ii)) was obtained, showing a structural peak in the higher q -value region ($0.5 \sim 1.0 \text{ nm}^{-1}$). This peak indicated that the hydrogel exhibited some structural order at this scale^[52,53], likely due to the high-coordinated Al³⁺ ions forming regularly arranged structural units. In the q -value range of $0.1 \sim 0.35 \text{ nm}^{-1}$, logarithmic fitting yielded surface and mass fractal dimensions (Figure 5(g–iii)). $D_s = 3.8$

suggested that the scattering objects (such as certain regions within the hydrogel network) had some surface roughness, while $D_m = 2.1$ indicated an uneven distribution of mass within the hydrogel^[54–56]. The presence of both fractal dimensions highlighted the complex, multi-scale structure of the Al-HG_{F1/F2} network at the nanoscale, thus a good energy dissipation system to obtain excellent mechanical properties.

3.4. Application of Al-HG_{F1/F2} in real-time rainfall monitoring

In this part, the promising application of Al-HG_{F1/F2} in real-time rainfall monitoring was evaluated. Before application, the biocompatibility, ionic conductivity, and sensing ability were assessed. First of all, according to the Cell Counting (Figure S5) and Live-Dead Cell Staining results (Figure S6), few dead NIH-3T3 cells were detected after incubating the cells with sample extract for 24, 72, and 120 h, indicating a good biocompatibility of Al-HG_{F1/F2}, manifesting as being environmentally benign and chemically stable. Such peculiarity was especially important for sensors exposed to natural environments over long periods. Subsequently, the ionic conductivity of Al-HG_{F1/F2} at 25 °C was calculated to be 0.9 S·m⁻¹ based on impedance spectra (Figure S7) measured by an electrochemical workstation. Such conductive property, comparable to that of reported metal ion coordination hydrogels^[57,58], rooted in the conductive media of free mobile ions (from aluminum salt), which could also lighten the LED bulb by designing a complete circuit using Al-HG_{F1/F2} as a wire to connect an LED bulb (Figure S8). When the Al-HG_{F1/F2} was stretched, the brightness of the LED bulb changed due to the weakness of the conductive network within the hydrogel during stretching. This phenomenon confirmed the potential of Al-HG_{F1/F2} as a flexible sensing material on account of its functional responsiveness. The sensing characteristics of Al-HG_{F1/F2} were further systematically studied, covering its sensitivity, response and recovery times, and durability as both a strain (Figure 6(a)) and pressure sensor (Figure 6(b)). For strain sensing, obvious changes in the relative resistance were observed at strain levels of 50%, 80%, 110%, and 140% (Figures 6(a-i)), demonstrating its sensing capability under various strain conditions. The sensitivity was further quantified using the gauge factor (GF) (Figure 6(a-ii)), which first decreased and then increased, but did not exceed the initial value within the strain ranges of 0%–45%, 45%–90%, and 90%–160%. This might be attributed to the conductive network undergoing a process from being intact, to partially disrupted, and then gradually reorganized. The average value of GF within the strain range of 0%–160% was 0.56, comparable to that of reported advanced conductive hydrogel sensors^[59,60], showing its good sensitivity. Moreover, the Al-HG_{F1/F2} strain sensor exhibited short response (85 ms) and recovery times (22 ms) (Figure 6(a-iii)), indicating its ability to quickly and accurately detect changes during stretching, making it suitable for real-time monitoring of dynamic changes. Under 100% strain, the sample was subjected to a rapid and continuous 1000-cycle stretching test (Figure 6(a-iv)). Similar to previously reported works^[61–63] that the resistance change rate showed no significant resistance drift or failure, the Al-HG_{F1/F2} demonstrated good cyclic

stability and durability, making it ideal for long-term strain sensing applications. The above results proved the excellent sensing sensitivity of the Al-HG_{F1/F2} hydrogel under ambient temperatures, and its sensing capability in a simulated rainwater environment was further evaluated. As shown in Figures 6(a–v), the resistance changes rate of the sample after soaking in rainwater was not significantly different from that of the unsoaked sample under the same strain conditions (Figures 6(a–i)), demonstrating that the Al-HG_{F1/F2} hydrogel exhibited good stability in a simulated rainwater environment, guaranteeing its practical application in real-time rainfall monitoring. Additionally, the results in Figure 6(b) showed that Al-HG_{F1/F2} also demonstrated promising potential as a pressure sensor.

To further validate the sensing performance of Al-HG_{F1/F2} in real rainwater monitoring, the sample was subject to soaking in the actual rainwater collected from Xi'an (Shaanxi, China). Similarly, the relative resistance change rates under tensile (Figure 7(a)) and compressive (Figure 7(b)) conditions illustrating its sensitivity, response, and recovery times were analyzed. Compared with the unsoaked samples (Figures 6(a) and (b)), the sensing ability showed no obvious difference after real rainwater soaking. Significantly, the rainwater-soaked Al-HG_{F1/F2} exhibited a relatively shorter tensile response time (61 ms) (Figure 7(a-iii)) and higher compressive sensitivity in the 0–20 kPa stress range (Figures 7(b-i)). These results indicated that Al-HG_{F1/F2} maintained good sensing performance after rainwater soaking, adapting well to real rainwater environments, with fast response characteristics and high stability. Such maintained or even improved sensing ability was attributed to its good mechanical properties even after rainwater soaking (Figure S9), suggesting that some components in rainwater positively modulated the gel network structure. This further confirmed the stability and usability of the Al-HG_{F1/F2} hydrogel in a rainwater environment.

Subsequently, the Al-HG_{F1/F2} sample was subjected to different rainfall intensities (simulated as light, moderate, heavy, and torrential rain). It could be found that the change rate of the relative resistance of the Al-HG_{F1/F2} varied significantly with different rainfall intensities and amounts (Figure 7(c)). As the rainfall intensity increased, the relative resistance change rate enhanced accordingly, showing excellent sensitivity. This indicated that the Al-HG_{F1/F2} sample could accurately detect rainfall intensity and convert it into a quantifiable resistance signal. In turn, by analyzing the range of the relative resistance change rates, it was possible to effectively distinguish between light, moderate, heavy, and torrential rain, highlighting the potential of the Al-HG_{F1/F2} hydrogel in rainwater monitoring systems. To verify the applicability of the Al-HG_{F1/F2} sample for real-time rainwater monitoring in different regions, the real rainwater collected from various climate zones of China including Northeast China (e.g. Heilongjiang), the North China Plain (e.g. Beijing), Central China (e.g. Hubei), and the Eastern Coastal City (e.g. Zhejiang) was used to simulate moderate rainfall intensity (Figure 7(d)). The results showed that, regardless of the rainwater sample source, the sensing ability remained stable, with no significant decline in performance, indicating that the Al-HG_{F1/F2} hydrogel had

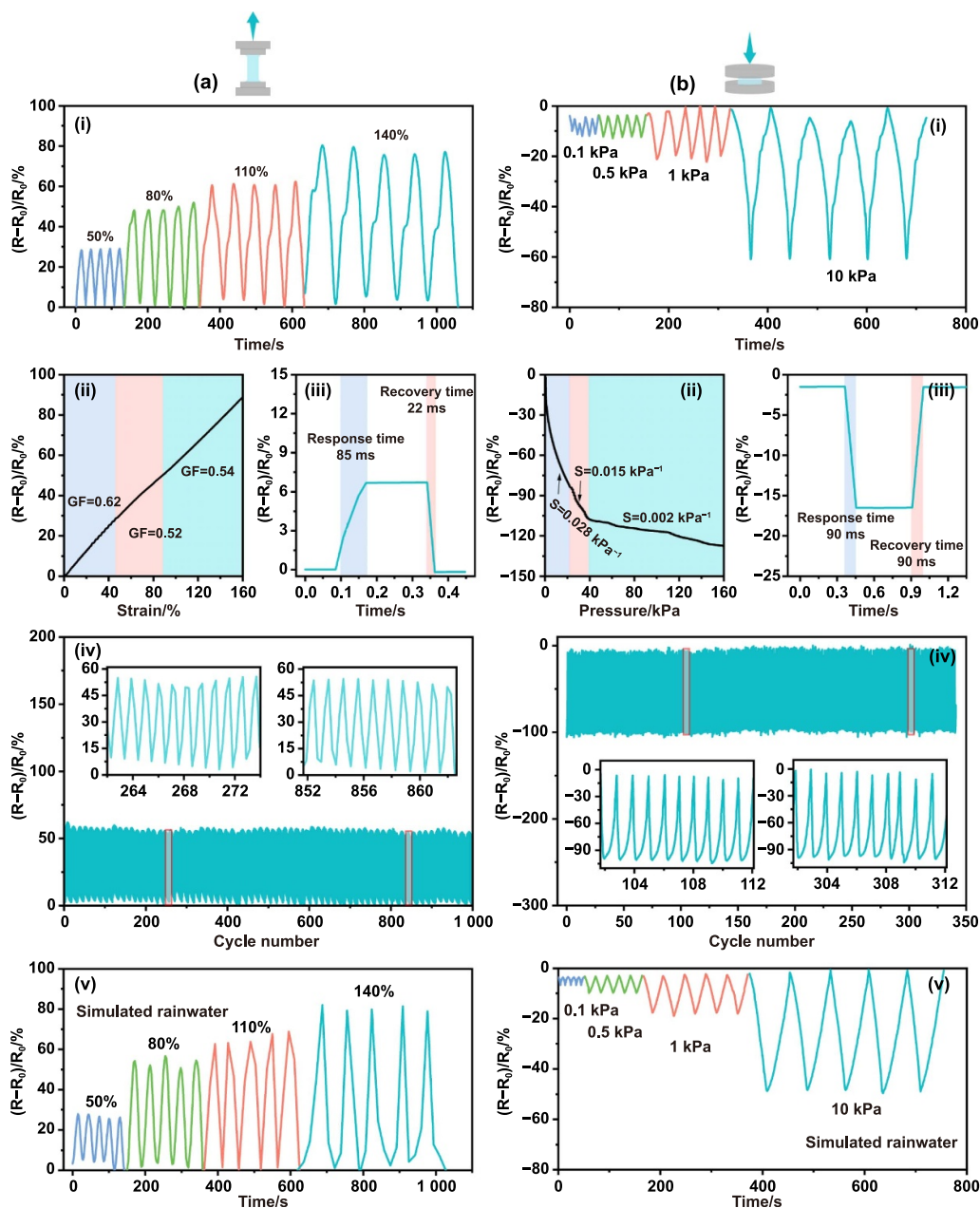


Figure 6. The change of relative resistance of the Al-HG_{F1/F2} under (a) tensile and (b) compression states: at different (a-i) strains and (b-i) stresses; (a-ii) gauge factor (GF, fitting correlation coefficient (R^2) > 0.999) and (b-ii) sensitivity (S , R^2 > 0.972); (a-iii) and (b-iii) the recovery/response time; (a-iv) and (b-iv) under consecutively cyclic operation; at different (a-v) strains and (b-v) stresses after the Al-HG_{F1/F2} sample immersion of 12 h in the simulated rainwater environments.

excellent adaptability to rainwater from different regions and could provide reliable monitoring capabilities under diverse environmental conditions. In addition to adapting to different regions and rainfall intensities, the Al-HG_{F1/F2} sample also maintained its rainfall monitoring capability under extreme conditions such as in low temperature, high temperature, hail-storm, and sunlight exposure, manifesting as the remained relatively stable GF values under these conditions (Figure S10). Its maintained reliable sensing performance across a wide range of temperature, impact, and light conditions made

the Al-HG_{F1/F2} an ideal sensing material for real-time rainfall monitoring applications, offering high reliability and long-lasting performance. Finally, real-time rainfall monitoring in Shaanxi University of Science and Technology (Xi'an, China) was conducted by constructing a model (Figure S11). As could be seen in Figure 7(e), over a monitoring period of 4 000 s, the change rate of the relative resistance of the Al-HG_{F1/F2} gradually decreased from the range of torrential rain intensity to that of moderate rain, closely matching the actual rainfall condition. This confirmed that the Al-HG_{F1/F2} sample exhibited

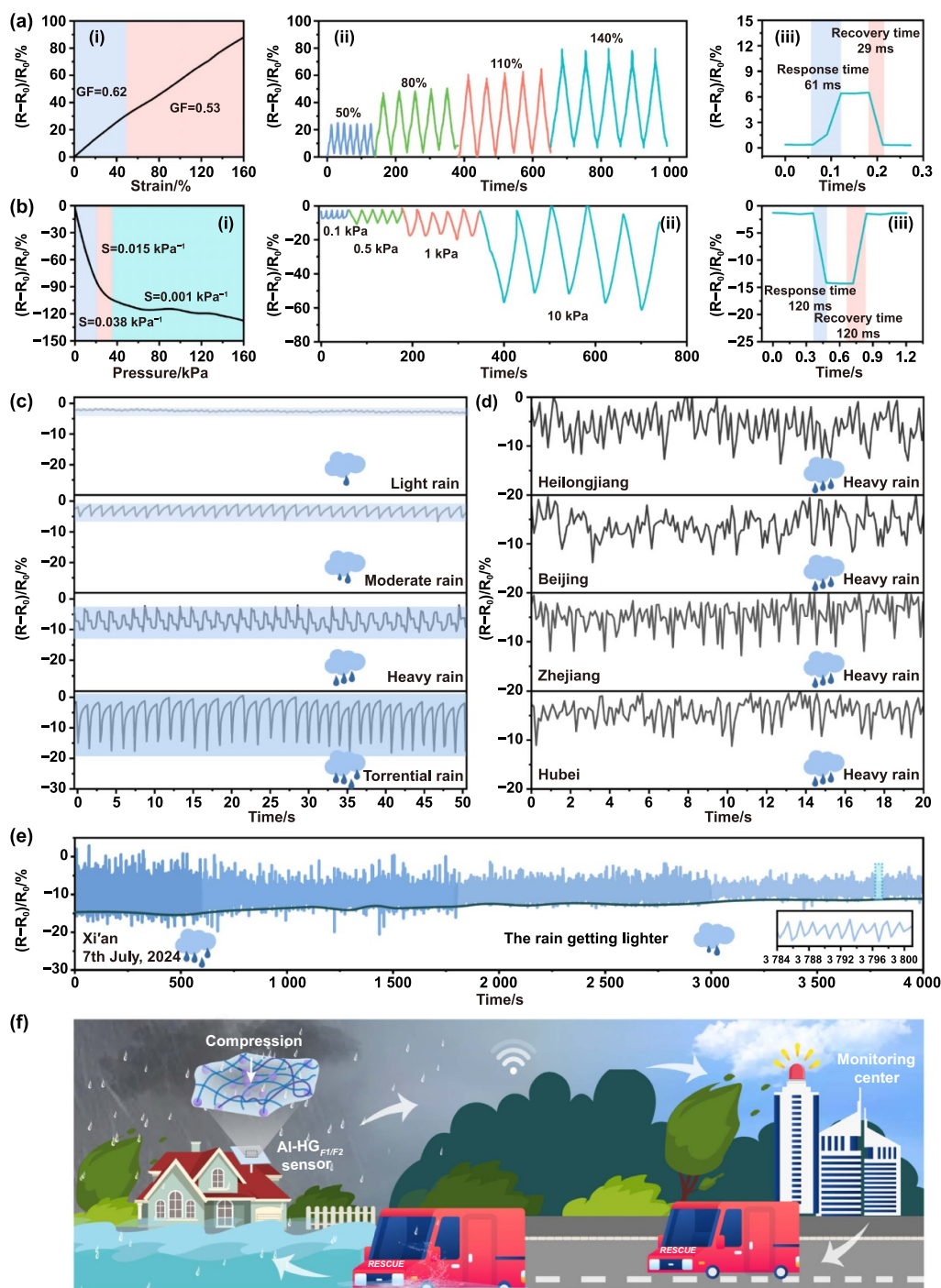


Figure 7. The real-time rainfall monitoring behavior. The change of relative resistance of the Al-HG_{F1/F2} after immersion of 12 h in the rainwater environments (Xi'an) under tensile (a) and compression (b) states: (a-i) gauge factor (GF, $R^2 > 0.999$) and (b-ii) sensitivity (S, $R^2 > 0.912$); at different (a-ii) strains and (b-ii) stresses; (a-iii) and (b-iii) the recovery/recovery time. The change of relative resistance under (c) different levels of rain, (d) different areas, (e) and real-time rainfall monitoring. (f) The scheme of rainfall monitoring mechanism and promising application of the Al-HG_{F1/F2} sensor in flood control and flood prevention.

high sensitivity and stability in real-world rainwater monitoring, which was significantly attributed to its excellent mechanical properties endowing by the novel low temperature induced strategy.

Based on the above results, it could be confirmed that the Al-HG_{F1/F2} sample, transferring the rainfall pressure into the

change of relative resistance (Figure 7(f)), displayed excellent response and recovery times, enabling rapid feedback and real-time monitoring. Moreover, its simple operation, low maintenance costs, and real-time data transmission capabilities allowed it to respond quickly to changes in rainfall conditions. These features enabled timely communication with relevant

authorities, providing a valuable time window for flood prevention and disaster mitigation, thus effectively supporting disaster response efforts (Figure 7(f)). In addition, the high sensitivity and real-time feedback capabilities of Al-HG_{F1/F2} made it highly promising in the field of environmental sensing, with particular value in addressing climate change and urban rainwater management.

4. Conclusions

In this work, inspired by the working mechanism of antifreeze proteins of Patagonian toothfish, a satisfactory aluminum coordination hydrogel (Al-HG_{F1/F2}) was successfully fabricated by a low-temperature induced strategy. Compared with the product by the traditional method (Al-HG_{F3/F0}), the mechanical performances covering compressive, tensile, puncture resistance, anti-fatigue, and anti-swelling of Al-HG_{F1/F2} were significantly improved. The low temperature promoted more and stronger ligand carboxyls firmly binding Al³⁺, thereby forming a high-coordinated structure, which was the mechanism for the enhanced mechanical properties of Al-HG_{F1/F2}. The good biocompatibility, ionic conductivity, and sensing ability, coupled with the excellent mechanical performances endowed Al-HG_{F1/F2} as a promising sensor for real-time rainfall monitoring in different regions, varied rainfall intensities, and even under extreme conditions. The simple operation, low deployment cost, flexibility, and instantaneity of rainfall monitoring made it a wide application prospect in flood prevention and disaster mitigation. Hence, this work highlighted the significant potential of low-temperature treatment in strengthening the performance of aluminum coordination hydrogel sensors and provided crucial insights for its development of future applications in rainfall monitoring.

Data availability statement

No data was used for the research described in the article.

Acknowledgment

This work was supported by the National Natural Science Foundation of China (22308210), the Young Talent Fund of the Association for Science and Technology in Shaanxi of China (20240412), the RIKEN-MOST Project between the Ministry of Science and Technology of the People's Republic of China (MOST) and RIKEN, the China Scholarship Council (202108610127), and the Natural Science Foundation of Shaanxi University of Science & Technology (2019BT-44).

Conflict of interest

The authors declare no conflict of interest.

ORCID iDs

Xiaoyu Guan  <https://orcid.org/0000-0003-4420-8770>
Yoshihiro Ito  <https://orcid.org/0000-0002-1154-253X>

References

- [1] Ouaadi N et al. 2024. Intercomparison of very high-resolution surface soil moisture products over Catalonia (Spain). *Remote Sens. Environ.* **309**, 114225.
- [2] Qiao X J, Peng T, Sun N, Zhang C, Liu Q L, Zhang Y, Wang Y H and Nazir M S. 2023. Metaheuristic evolutionary deep learning model based on temporal convolutional network, improved aquila optimizer and random forest for rainfall-runoff simulation and multi-step runoff prediction. *Expert Syst. Appl.* **229**, 120616.
- [3] Liu Q L, Jian W B and Nie W. 2021. Rainstorm-induced landslides early warning system in mountainous cities based on groundwater level change fast prediction. *Sustain. Cities Soc.* **69**, 102817.
- [4] Li G, Li C L, Li G D, Yu D H, Song Z P, Wang H L, Liu X N, Liu H and Liu W X. 2022. Development of conductive hydrogels for fabricating flexible strain sensors. *Small* **18**, 2101518.
- [5] Hu L X et al. 2023. Hydrogel-based flexible electronics. *Adv. Mater.* **35**, 2205326.
- [6] Zeng Z F, Yang Y Q, Pang X W, Jiang B Y, Gong L X, Liu Z L, Peng L and Li S N. 2024. Lignin nanosphere-modified MXene activated-rapid gelation of mechanically robust, environmental adaptive, highly conductive hydrogel for wearable sensors application. *Adv. Funct. Mater.* **34**, 2409855.
- [7] Qi H N, Jing X L, Hu Y L, Wu P, Zhang X J, Li Y T, Zhao H K, Ma Q L, Dong X T and Mahadevan C K. 2025. Electrospun green fluorescent-highly anisotropic conductive Janus-type nanoribbon hydrogel array film for multiple stimulus response sensors. *Composites B* **288**, 111933.
- [8] Yan L W, Zhou T, Han L, Zhu M Y, Cheng Z, Li D, Ren F Z, Wang K F and Lu X. 2021. Conductive cellulose bionanosheets assembled biostable hydrogel for reliable bioelectronics. *Adv. Funct. Mater.* **31**, 2010465.
- [9] Cui W, Zheng Y, Zhu R J, Mu Q F, Wang X Y, Wang Z S, Liu S Q, Li M and Ran R. 2022. Strong tough conductive hydrogels via the synergy of ion-induced cross-linking and salting-out. *Adv. Funct. Mater.* **32**, 2204823.
- [10] Cheng T, Zhang Y Z, Wang S, Chen Y L, Gao S Y, Wang F, Lai W Y and Huang W. 2021. Conductive hydrogel-based electrodes and electrolytes for stretchable and self-healable supercapacitors. *Adv. Funct. Mater.* **31**, 2101303.
- [11] Zhang H Y, Yang Q N, Xu L J, Li N, Tan H H, Du J J, Yu M L and Xu J X. 2024. Triboelectric nanogenerators based on hydrated lithium ions incorporated double-network hydrogels for biomechanical sensing and energy harvesting at low temperature. *Nano Energy* **125**, 109521.
- [12] Guan X Y et al. 2024. Mineral tanning-inspired metal ions coordination hydrogels with outstanding mechanical strength and toughness for flexible force sensors. *Adv. Funct. Mater.* **34**, 2313633.
- [13] Guan X Y et al. 2024. Shutters-Inspired metal ions coordination hydrogel Strain/Pressure sensor for joint behavior evaluation and flatfoot correction. *Chem. Eng. J.* **489**, 151353.
- [14] Jiang Y Z, Venkatesan H, Shi S, Wang C, Cui M, Zhang Q, Tan L and Hu J L. 2023. Spider-capture-silk mimicking fibers with high-performance fog collection derived from

- superhydrophilicity and volume-swelling of gelatin knots. *Collagen Leather* **5**, 4.
- [15] Ambekar R S, Kushwaha B, Sharma P, Bosia F, Fraldi M, Pugno N M and Tiwary C S. 2021. Topologically engineered 3D printed architectures with superior mechanical strength. *Mater. Today* **48**, 72–94.
- [16] Lian Z Z, Zhou J H, Ren W F, Chen F Z, Xu J K, Tian Y L and Yu H D. 2024. Recent progress in bio-inspired macrostructure array materials with special wettability—from surface engineering to functional applications. *Int. J. Extrem. Manuf.* **6**, 012008.
- [17] Thosar A U, Shalom Y, Braslavsky I, Drori R and Patel A J. 2023. Accumulation of antifreeze proteins on ice is determined by adsorption. *J. Am. Chem. Soc.* **145**, 17597–17602.
- [18] Ampaw A. 2022. Antifreeze proteins solve cold problems. *Nat. Chem.* **14**, 1336.
- [19] Deleray A C, Saini S S, Wallberg A C and Kramer J R. 2024. Synthetic antifreeze glycoproteins with potent ice-binding activity. *Chem. Mater.* **36**, 3424–3434.
- [20] Zhang Y, Jiao L, Yang W J, Xie C F and Jiang H L. 2021. Rational fabrication of low-coordinate single-atom Ni electrocatalysts by MOFs for highly selective CO₂ reduction. *Angew. Chem., Int. Ed.* **60**, 7607–7611.
- [21] Li Y X and Xie X M. 2023. One-step synthesis of intelligent ionohydrogels toughened with carboxyl-Al³⁺ coordination facilitated by ionic liquids. *Polymer* **283**, 126223.
- [22] Li H J, Zheng H, Tan Y J, Tor S B and Zhou K. 2021. Development of an ultrastretchable double-network hydrogel for flexible strain sensors. *ACS Appl. Mater. Interfaces* **13**, 12814–12823.
- [23] Huang C, Miao Q Q, Chen Y H, Zhang Q, He X, Li L and Liu X G. 2022. Highly robust, sensitive, antifreezing, and drying-tolerant polyacrylamide/gelatin/Zr⁴⁺ hydrogels as flexible strain sensors. *ACS Appl. Polym. Mater.* **4**, 8613–8622.
- [24] Li B, Li Z Q and Li H R. 2022. Ultrastretchable luminescent nanocomposite hydrogel with self-healing behavior. *ACS Appl. Polym. Mater.* **4**, 2329–2336.
- [25] Huang Y W, Xiao L Y, Zhou J, Liu T, Yan Y Q, Long S J and Li X F. 2021. Strong tough polyampholyte hydrogels via the synergistic effect of ionic and metal-ligand bonds. *Adv. Funct. Mater.* **31**, 2103917.
- [26] Li R R, Ren J, Zhang M M, Li M, Li Y and Yang W. 2024. Highly stretchable, fast self-healing, self-adhesive, and strain-sensitive wearable sensor based on ionic conductive hydrogels. *Biomacromolecules* **25**, 614–625.
- [27] Choi S, Choi Y and Kim J. 2019. Anisotropic hybrid hydrogels with superior mechanical properties reminiscent of tendons or ligaments. *Adv. Funct. Mater.* **29**, 1904342.
- [28] Li T T, Hu X M, Zhang Q S, Zhao Y Y, Wang P, Wang X, Qin B T and Lu W. 2020. Poly(acrylic acid)-chitosan @ tannic acid double-network self-healing hydrogel based on ionic coordination. *Polym. Adv. Technol.* **31**, 1648–1660.
- [29] Liu Z X, Liang G J, Zhan Y X, Li H F, Wang Z F, Ma L T, Wang Y K, Niu X R and Zhi C Y. 2019. A soft yet device-level dynamically super-tough supercapacitor enabled by an energy-dissipative dual-crosslinked hydrogel electrolyte. *Nano Energy* **58**, 732–742.
- [30] Pan J Z, Jin Y, Lai S Q, Shi L J, Fan W H and Shen Y C. 2019. An antibacterial hydrogel with desirable mechanical, self-healing and recyclable properties based on triple-physical crosslinking. *Chem. Eng. J.* **370**, 1228–1238.
- [31] Zhang J C, Zhuang J S, Lei L R and Hou Y. 2023. Rapid preparation of a self-adhesive PAA ionic hydrogel using lignin sulfonate-Al³⁺ composite systems for flexible moisture-electric generators. *J. Mater. Chem. A* **11**, 3546–3555.
- [32] Jiang H Y, Fan L X, Yan S, Li F B, Li H J and Tang J G. 2019. Tough and electro-responsive hydrogel actuators with bidirectional bending behavior. *Nanoscale* **11**, 2231–2237.
- [33] Yin J Y, Pan S X, Wu L L, Tan L Y N, Chen D, Huang S, Zhang Y H and He P X. 2020. A self-adhesive wearable strain sensor based on a highly stretchable, tough, self-healing and ultra-sensitive ionic hydrogel. *J. Mater. Chem. C* **8**, 17349–17364.
- [34] Zheng W J, An N, Yang J H, Zhou J X and Chen Y M. 2015. Tough Al-alginate/poly(*N*-isopropylacrylamide) hydrogel with tunable LCST for soft robotics. *ACS Appl. Mater. Interfaces* **7**, 1758–1764.
- [35] Zhang Z, Wang X D, Liu T, Liu L, Yu C L, Tian Y L, Zhang X X and Shen J. 2022. Al³⁺ coordinated chitosan hydrogel with ultrahigh water absorbency and environmental response. *Mater. Des.* **214**, 110390.
- [36] Sun Y F, Thakur V K and Luo R. 2024. High mechanical strength, strong adhesion, self-healing and conductive ionic hydrogels for motion detection. *Polymer* **299**, 126946.
- [37] Jiang H Y, Hao Z X, Zhang J F, Tang J G and Li H J. 2023. Bioinspired swelling enhanced hydrogels for underwater sensing. *Colloids Surf. A* **664**, 131197.
- [38] Li Z X, Chen J Y, Wu Y, Huang Z Y, Wu S T, Chen Y, Gao J, Hu Y and Huang C. 2022. Effect of downstream processing on the structure and rheological properties of xanthan gum generated by fermentation of *Melaleuca alternifolia* residue hydrolysate. *Food Hydrocoll.* **132**, 107838.
- [39] Hafeez S, Aldana A A, Duimel H, Ruiter F A A, Decarli M C, Lapointe V, van Blitterswijk C, Moroni L and Baker M B. 2023. Molecular tuning of a benzene-1,3,5-tricarboxamide supramolecular fibrous hydrogel enables control over viscoelasticity and creates tunable ECM-mimetic hydrogels and bioinks. *Adv. Mater.* **35**, 2207053.
- [40] Zhao C K et al. 2023. Nanofibrous polypeptide hydrogels with collagen-like structure as biomimetic extracellular matrix. *Collagen Leather* **5**, 3.
- [41] Hughes S M, Aykanat A, Pierini N G, Paiva W A, Weeks A A, Edwards A S, Durant O C and Oldenhuis N J. 2024. DNA-intercalating supramolecular hydrogels for tunable thermal and viscoelastic properties. *Angew. Chem., Int. Ed.* **63**, e202411115.
- [42] Zhang J et al. 2023. All-organic polymeric materials with high refractive index and excellent transparency. *Nat. Commun.* **14**, 3524.
- [43] Eklund A, Zhang H, Zeng H, Priimagi A and Ikkala O. 2020. Fast switching of bright whiteness in channeled hydrogel networks. *Adv. Funct. Mater.* **30**, 2000754.
- [44] Lyu Y, Guo R, Lin Z W, Zhai F, Wu T, Jiang P, Ji Z Y, Ma S H, Shi X Y and Wang X L. 2023. Ion clusters-driven strong and acid/alkali/ freezing-tolerant conductive hydrogels for flexible sensors in extreme environments. *Adv. Funct. Mater.* **33**, 2306300.
- [45] Guo X, Dong X Y, Zou G J, Gao H J and Zhai W. 2023. Strong and tough fibrous hydrogels reinforced by multiscale hierarchical structures with multimechanisms. *Sci. Adv.* **9**, eadf7075.
- [46] Xu L J, Qiao Y and Qiu D. 2023. Coordinatively stiffen and toughen hydrogels with adaptable crystal-domain crosslinking. *Adv. Mater.* **35**, 2209913.
- [47] Ma J Z, Cheng Z J, Tan S, Zheng T and Zong Y. 2023. High performance strain sensor based on leather activated by micro-cracking conductive layer. *Collagen Leather* **5**, 25.
- [48] Peng F L et al. 2023. Guided bone regeneration in long-bone defect with a bilayer mineralized collagen membrane. *Collagen Leather* **5**, 36.
- [49] Jiang Z B et al. 2023. Manufacturing N,O-carboxymethyl chitosan-reduced graphene oxide under freeze-drying for performance improvement of Li-S battery. *Int. J. Extrem. Manuf.* **5**, 015502.
- [50] Wychowaniec J K, Iliut M, Borek B, Muryn C, Mykhaylyk O O, Edmondson S and Vijayaraghavan A. 2021. Elastic flow

- instabilities and macroscopic textures in graphene oxide lyotropic liquid crystals. *npj 2DMater. Appl.* **5**, 11.
- [51] Manca M, Zhang C, de Melo Freire R V, Scheffold F and Salentinig S. 2023. Single particle investigation of triolein digestion using optical manipulation, polarized video microscopy, and SAXS. *J. Colloid Interface Sci.* **649**, 1039–1046.
- [52] Vislavath P, Billa S, Bahadur S P, Sudarshan J, Patro K, Tu R S K and Ratna D. 2022. Heterogeneous coordination environment and unusual self-assembly of ionic aggregates in a model ionomeric elastomer: effect of curative systems. *Macromolecules* **55**, 6739–6749.
- [53] Rahmati M et al. 2022. Intrinsically disordered peptides enhance regenerative capacities of bone composite xenografts. *Mater. Today* **52**, 63–79.
- [54] Zhang Q, Liu Y R, Li X C, Nie B S and Meng J Q 2023. Research on mechanical properties of loaded coal at the micro/nanoscale by coupling nanoindentation and SAXS experiments.
- [55] Huang T F et al. 2024. Performance and solution structures of side-chain-bridged oligo (ethylene glycol) polymer photocatalysts for enhanced hydrogen evolution under natural light illumination. *Small* **20**, 2304743.
- [56] Xu J C, Li Z H, Zhong Y Y, Zhou Q, Lv Q, Chen L, Blennow A and Liu X X. 2021. The effects of molecular fine structure on rice starch granule gelatinization dynamics as investigated by *in situ* small-angle x-ray scattering. *Food Hydrocoll.* **121**, 107014.
- [57] Chen D W, Bai H Y, Zhu H Y, Zhang S W, Wang W and Dong W F. 2024. Anti-freezing, tough, and stretchable ionic conductive hydrogel with multi-crosslinked double-network for a flexible strain sensor. *Chem. Eng. J.* **480**, 148192.
- [58] Liu Y, Wang J, Hou P, Gao Z C, Liu Y, Zhao J N and Huo P F. 2024. Preparation of dual cross-linked hydrogel electrolytes containing modified lignin for supercapacitors and sensors. *Chem. Eng. J.* **480**, 148259.
- [59] Kim T, Park C, Samuel E P, An S, Aldalbahi A, Alotaibi F, Yarin A L and Yoon S S. 2021. Supersonically sprayed washable, wearable, stretchable, hydrophobic, and antibacterial rGO/AgNW fabric for multifunctional sensors and supercapacitors. *ACS Appl. Mater. Interfaces* **13**, 10013–10025.
- [60] Wang X F, Li X C, Wang B B, Chen J C, Zhang L, Zhang K, He M, Xue Y and Yang G H. 2022. Preparation of salt-induced ultra-stretchable nanocellulose composite hydrogel for self-powered sensors. *Nanomaterials* **13**, 157.
- [61] Miao C, Li P H, Yu J D, Xu X W, Zhang F and Tong G L. 2023. Dual network hydrogel with high mechanical properties, electrical conductivity, water retention and frost resistance, suitable for wearable strain sensors. *Gels* **9**, 224.
- [62] Zhang Z L et al. 2023. Fatigue-resistant conducting polymer hydrogels as strain sensor for underwater robotics. *Adv. Funct. Mater.* **33**, 2305705.
- [63] Cheng Y G et al. 2024. Chrysalis-inspired high-toughness low-modulus conductive hydrogel sensor for intelligent sensing. *Chem. Eng. J.* **498**, 155475.